Microscopy-based chromosome conformation capture enables simultaneous visualization of genome organization and transcription in intact organisms

Andrés M. Cardozo Gizzi[1,✣], Diego I. Cattoni[1], Jean-Bernard Fiche[1], Sergio Espinola[1], Julian Gurgo[1], Olivier Messina[1], Christophe Houbron[1], Yuki Ogiyama[2], Giorgio-Lucio Papadopoulos[2], Giacomo Cavalli[2], Mounia Lagha[3], Marcelo Nollmann [1,#]

[1] *Centre de Biochimie Structurale, CNRS UMR 5048, INSERM U1054, Université de Montpellier, 60 rue de Navacelles, 34090, Montpellier, France*

[2] *Institut de Génétique Humaine, CNRS UMR 9002, Université de Montpellier, 141 rue de la Cardonille, 34396, Montpellier, France*

[3] *Institut de Génétique Moléculaire de Montpellier, CNRS UMR 5535, Université de Montpellier, 1919 Route de Mende, 34293, Montpellier, France*

✣ *present address: CIQUIBIC (CONICET) – Departamento de Química Biológica Ranwel Caputto, Facultad de Ciencias Químicas, Universidad Nacional de Córdoba, Haya de la Torre y Medina Allende, Ciudad Universitaria, 5000, Córdoba, Argentina.*

[#] To whom correspondence should be addressed:

Marcelo Nollmann: marcelo.nollmann@cbs.cnrs.fr

Abstract

Eukaryotic chromosomes are organized in multiple scales, from nucleosomes to chromosome territories. Recently, genome-wide methods identified an intermediate level of chromosome organization, topologically associating domains (TADs), that play key roles in transcriptional regulation. However, these methods cannot directly examine the interplay between transcriptional activation and chromosome organization while maintaining spatiotemporal information. Here, we present a multiplexed, sequential imaging approach (Hi-M) that permits the simultaneous detection of chromosome organization and transcription in single nuclei. We used Hi-M to study chromosome organization during the awakening of the zygotic genome in intact *Drosophila* embryos. By visualizing chromosome architecture and gene expression simultaneously in single nuclei, we were able to unveil the changes in 3D chromatin organization occurring upon transcriptional activation and homologous chromosome un-pairing. Excitingly, the ability of Hi-M to explore the multi-scale chromosome architecture in time and space will be key to understand the mechanisms and consequences of the 4D organization of the genome.

Introduction

The study of chromosome organization and transcriptional regulation has been recently revolutionized by the advent of genome-wide sequencing methods. In particular, chromosome conformation capture technologies, such as Hi-C, have revealed that eukaryotic chromosomes are organized into topological-associating domains (Dixon et al. 2012; Nora et al. 2012; Sexton et al. 2012) that can interact together to form active or repressed compartments (Lieberman-Aiden et al. 2009; Dixon et al. 2015). Importantly, disruption of TAD architecture leads to developmental pathologies and disease due to improper gene regulation (Spielmann, Lupiáñez, and Mundlos 2018; Hnisz et al. 2016; Dixon, Gorkin, and Ren 2016). Thus, determining the role of chromatin architecture in gene regulation has become a key issue in the fields of chromatin biology and transcription.

Recently, single-cell Hi-C and imaging studies showed that chromosomal contacts within and between TADs are highly stochastic and occur at surprisingly low frequencies (Nagano et al. 2017; Flyamer et al. 2017; Stevens et al. 2017; Cattoni et al. 2017). The origin of these heterogeneities has been unclear and may arise from multiple sources, such as variations in transcriptional and/or epigenetic state between cells within multicellular organisms or in cell cultures. Up until now, it has been difficult to detect the origin of these variations, as methods that are able to detect transcriptional output and chromosome organization simultaneously at the single cell level and in the context of an organism have been lacking. In part, this is due to the loss of spatial information in sequencing-based methods.

The study of chromatin architecture and organization by microscopy is limited by several factors. In conventional fluorescence *in situ* hybridization (FISH), the number of spectrally-distinguishable fluorophores in standard microscopes limits the

maximum number of genomic loci that can be simultaneously imaged (usually <4). In addition, FISH probes are typically large (>10kb) and difficult to construct, at least in large numbers. These limitations impose a lower limit on the genomic coverage achievable by FISH. Newly developed, low-cost, high-efficiency on-chip DNA synthesis for high coverage FISH (oligopaint) have been used to directly label and image entire TADs (Beliveau et al. 2015; Boettiger et al. 2016; Szabo et al. 2018) or TAD borders (Cattoni et al. 2017). These technologies have been recently combined with multiplexed sequential optical imaging to detect hundreds of individual RNA species while still maintaining spatial information (Kok Hao Chen et al. 2015; Moffitt et al. 2016; Eng et al. 2017; Shah et al. 2018), as well as to visualize the segregation of TADs into chromosome territories (Wang et al. 2016). These methods, however, lacked the genomic resolution to detect TADs and to correlate them with transcriptional activity in the context of intact tissues or organisms.

To overcome these limitations, we introduce a high-throughput, high-resolution, high-coverage microscopy-based technology (Hi-M), capable of simultaneously detecting RNA expression and 3D chromatin organization at the single-cell level with nanometer and kilobase resolutions in intact *Drosophila melanogaster* embryos. We used Hi-M to visualize the emergence of TADs during the awakening of the zygotic genome. In addition, we found that TAD organization was disrupted during mitosis, and detected the changes in chromatin organization upon chromosome un-pairing. Finally, we show that the internal organization of TADs change upon transcriptional activation.

Results

Hi-M: a multicolor high-throughput, multiplexed microscopy and image analysis technology to map gene expression and capture chromosome conformation in single cells

Hi-M microscopy relies on the high-throughput, sequential labeling and imaging of multiple DNA loci in genomic regions spanning hundreds of kilobases (kb). DNA was labeled using oligopaint technologies (Beliveau et al. 2012, 2015). A primary library containing thousands of oligonucleotides targeting multiple genomic loci was designed and produced by high-throughput DNA synthesis (Methods). The subset of oligonucleotides targeting each genomic locus (hereafter barcode) contained unique tails with specific sequences that could be independently read by complementary, fluorescently-labeled oligonucleotide probes (hereafter readout probes; Figures 1A, S1A). An additional barcode (hereafter fiducial barcode), visible in all rounds of hybridization, was used for image registration and drift correction (Methods).

Barcodes were imaged using a robotic, fully-automated, four-color microscope coupled to an automated microfluidics system. Dozens of embryos were attached to a poly-L-lysine-coated coverslip and mounted into a microfluidics chamber (Methods, Figure 1B). The imaging registration phase involved the acquisition of four channel, 3D images of each entire embryo in the chamber to identify embryonic morphology (bright field), nuclei by DAPI staining (blue channel), RNA expression patterns (green channel) and detect the positions of fiducial barcodes (yellow channel, Methods) (Figures 1C and S1B). Next, we performed multiple sequential cycles of hybridization, washing, and imaging of each barcode using a dedicated fluid handling system (Figures 1B-C, Methods). For each hybridization cycle, we performed 3D,

two-color imaging of readout probes and fiducial barcodes (Figures 1C and S1A-B and Methods). Sample drift during acquisition was corrected using the fiducial barcode (Figures S1D-E and Methods). The overall labeling efficiency was over 60% and did not vary considerably between hybridization cycles (Figure S1F). A custom-made analysis pipeline was developed for semi-automated image processing and analysis (Methods).

Hi-M enables visualization of chromosome structure with high coverage and high resolution

We applied Hi-M to study chromosome organization during early Drosophila development at the time of zygotic genome activation (ZGA). To this purpose, we initially focused on a genomic locus containing the snail (*sna*) and escargot (*esg*) genes, which are among the ~100 genes expressed during the first wave of ZGA as early as stage 4 (nuclear cycles, nc, 10-13) (K. Chen et al. 2013). *Sna* and *esg* genes encode zinc finger transcription factors, essential for a variety of processes such as gastrulation, neuroblast specification or stem cell maintenance (Korzelius et al. 2014; Ashraf et al. 1999). In nc 14, the genomic locus encompassing these genes folds into a well-defined TAD (Ogiyama et al. 2018) demarcated by two borders containing class I insulators (CTCF, Beaf-32 and CP190)(Nègre et al. 2010) and housekeeping genes (Figure 1D). To study the 3D organization of this locus by Hi-M, we designed an oligopaint library covering the whole locus with an average distance between barcodes of 17 kb (Figure 1D). This primary library consisted of 2,000 different 142-base pairs oligonucleotides targeting 22 loci around *sna* (21 barcodes and a fiducial barcode).

We performed Hi-M experiments on the *sna-esg* locus in *Drosophila* embryos in nc 14. To validate the method, we first measured the mean physical distances and the absolute probability of interaction between any two loci as a function of their genomic distance. These data overlay well with our recent pairwise distance and absolute contact frequency measurements using super-resolution microscopies (Cattoni, et al 2017) (Figures 1E-F). It is worth noting that a Hi-M dataset provides a much larger coverage for both types of measurements while being much less time consuming (2 days versus ~1 year for the datasets displayed in Figures 1E-F).

Next, we constructed a contact probability map from our Hi-M dataset and compared it with published Hi-C data interpolated at the barcodes positions (Figures 1G, S1G and Methods) from equivalent Drosophila embryonic stages (Ogiyama et al. 2018). Remarkably, we observed a qualitative and quantitative agreement between these two interaction maps (Figures 1G and S1H, Pearson coefficient = 0.91). Two clearly distinguishable TADs are visible in this locus for both matrices (TAD-1, TAD-2, Figure 1D). TAD-1 contains the *sna* and *esg* genes, and is separated from TAD-2 by a barrier containing highly-expressed housekeeping genes, RNA pol II, class I insulator proteins, and Zelda (Figures 1G, S4A).

To further characterize chromatin organization in this locus, we built normalized contact and distance maps (Figures 1H-I). The normalized contact map showed enriched interactions within each of the two TADs detected by genomic methods (Figure 1H, dashed boxes) and depleted interactions at TAD borders (Figure 1H, green arrow). Interestingly, pairwise distances within TADs were smaller than expected whereas pairwise distances of loci at TAD borders were higher. Thus, the chromatin fiber is condensed within TADs and decondensed in TAD borders (Figure 1I, dashed boxes and red arrows, respectively).

Chromosome structure in paired and unpaired chromosomes

Drosophila chromosomes display a high degree of homologous pairing in somatic cells (Fung et al. 1998; Joyce et al. 2012). Thus, an important unanswered question is whether chromosome architecture is influenced by pairing. This question cannot be answered by genome-wide methods as they are unable to distinguish between inter- and intra-chromosomal contacts. We took advantage of the capability of Hi-M to discern paired and unpaired chromosomes to compare chromatin structure in each configuration. In our Hi-M data, homologous pairing was ~70 % for nc 14 nuclei (Figure S2A), in good agreement with previously published results (Fung et al. 1998; Cattoni et al. 2017). Normalized distance maps and contact matrices for paired and unpaired chromosomes were qualitatively very similar (Figures 2A and S2B-C). To quantitatively compare these two configurations, we performed a multi-scale correlation analysis of Hi-M distance maps (Methods). This analysis revealed that Hi-M matrices are almost identical (correlation = 1) at low resolution and retained a large, although reduced, similarity even at the highest resolution (correlation = 0.6, Figure 2B). This indicates that the overall organization of chromatin into TADs is similar in paired and unpaired chromosomes. Consistently with this picture, mean pairwise distances between paired and unpaired chromosomes were highly correlated (Figure 2C). To our surprise, however, pairwise distances in unpaired chromosomes were in most cases larger than in paired chromosomes, indicating that chromatin in unpaired chromosomes is less compact. Overall, these results suggest that chromatin folding into TADs is similar between paired and unpaired chromosomes but there is an overall decompaction upon chromosome un-pairing.

Chromosome organization changes during cell-cycle and development

Recent genome-wide studies showed that chromosome organization into TADs changes during the cell cycle (Naumova et al. 2013; Nagano et al. 2017; Hug et al. 2017). To study whether we could observe such changes by microscopy, we performed Hi-M in embryos undergoing mitosis (Figure 3A). We observed that TADs were no longer discernible at this phase of the cell cycle and that the frequency of genomic contacts was almost independent of genomic distance at short scales (<400 kb, Figures 3B-D, S3B), reflecting a lack of hierarchical organization during mitosis. Overall, these results are in excellent agreement with published Hi-C data in (Naumova et al. 2013; Nagano et al. 2017; Hug et al. 2017) (Figures 3B, S3A). Normalized distance maps indicate a low correlation between physical and genomic distances (Figure 3D), consistent with irregular, intermingled loops forming a uniform-density, phase-like structure as previously proposed (Nishino et al. 2012; Naumova et al. 2013).

Next, we used Hi-M to investigate whether chromosome organization changed during the mid-blastula transition (MBT) at the onset of the major wave of zygotic transcription occurring at nc 14. For this, we performed Hi-M in embryos in nc 12-13 (pre-MBT) and nc 14 (MBT) (Figures 3E, 3I). Hi-M maps displayed a good correspondence with Hi-C maps (Figures 3F-G, 3J-K). Notably, TADs emerged at the onset of the ZGA (Figures 3G, 3K), consistent with previous Hi-C studies (Figures 3F, 3J, and S3A) (Hug et al. 2017; Ogiyama et al. 2018). Hi-M contact frequencies decayed more dramatically with genomic distance in nc 14 than in previous nuclear cycles, consistent with a change in the overall organization of the chromatin fiber occurring at this stage (Figures S3B). These local changes in chromatin organization were also clearly seen in normalized mean distance maps, where a progressive

condensation of chromatin in TADs between nc 12-13 and nc 14 can be observed (Figures 3H and 3L).

Simultaneous measurement of TAD organization and transcriptional activity in single nuclei

Several studies correlating chromosome organization and transcription have suggested that TAD organization changes upon transcriptional activation (Hug et al. 2017; Phanstiel et al. 2017; Stadhouders et al. 2018; Cruz-Molina et al. 2017). However, due to intrinsic limitations in Hi-C technologies, it has been so far impossible to detect chromosome organization and transcriptional state at the same time in single cells. We set out to test whether Hi-M could be adapted to perform this measurement. For this, we included an RNA labeling step in our imaging pipeline (Methods) that allows us to detect which nuclei in the embryo are transcriptionally active (Figure 4A). Specifically, we labeled and imaged *sna* transcripts in whole embryos, and detected its characteristic ventral expression pattern in nc 14 (Alberga et al. 1991) (Figure 4A).

Hi-C maps at the *sna* locus contains two TADs (TAD-1 and TAD-2), with TAD-1 displaying looping interactions between regions surrounding *sna* and *esg* (Figure S4A). Surprisingly, TAD-1 could be clearly discerned in nuclei where *sna* was repressed but not in transcriptionally active nuclei (Figures 4B-C). This observation strongly suggests that chromatin organization into TADs is disrupted by transcriptional activation.

To gain further insight into the structural changes that may underpin this difference in TAD organization, we calculated the normalized median distance maps for *sna* positive nuclei and for their neighbouring inactive nuclei. The patterns of

chromatin folding within the largest TAD (containing *sna*) showed clear changes upon *sna* expression (Figures 4D-E, S4B). Strikingly, chromatin structure in the vicinity of *sna* was locally decondensed in nuclei exhibiting active *sna* transcription. In nc 14, the expression patterns of *sna* and *esg* do not overlap in space (Hemavathy et al. 2004). Thus, the local chromatin decondensation in the vicinity of *esg* in nuclei that are not transcribing *sna* is consistent with active *esg* transcription leading to local chromatin decondensation.

Hi-C maps from nc 14 display specific looping interactions between regions surrounding *esg* and *sna* (Figure S4A). However, Hi-C cannot discern whether these contacts depend on the transcriptional status of these genes. Surprisingly, Hi-M revealed that genomic regions around *sna* and *esg* are closer than expected in both actively transcribing and inactive nuclei (Figures 4D-E, S4B). Exploration of existing Chip-seq datasets showed that the region surrounding and encompassing these genes is occupied by active (GAGA-factor, Zelda, CP190)(Blythe and Wieschaus 2016) as well as inactive marks (Polycomb group proteins, H3K27me3) (Figure S4C). Thus, we hypothesize that different networks of contacts are responsible for the distinct patterns of interactions visualized by Hi-M in active and inactive nuclei.

Conclusions

We developed a new method — Hi-M — based on sequential, multiplexed, high-throughput hybridization and imaging of oligopaint probes to visualize chromosome organization and transcriptional activity simultaneously in single cells while preserving tissue context. We validated our method by comparing our results with existing microscopy and Hi-C datasets, and demonstrated the many advantages of Hi-M by revealing: (1) the changes in chromosome organization during un-pairing of homologous chromosomes, (2) the disruption of TADs during mitosis, (3) the

emergence of TADs at the onset of the ZGA during embryonic development, and (4) the dramatic changes in TAD architecture upon transcriptional activation. In addition, Hi-M opens many new possibilities, such as the determination of genome organization at different mitotic stages (prophase, metaphase, anaphase) to decipher at which of these stages TAD organization is regained and the mechanisms involved in this process. Excitingly, Hi-M can be widely applied to detecting single-cell chromosome organization and transcription in cultured cells, from bacteria to mammals, or in multicellular organisms and tissues. Thus, this novel technology has the potential to revolutionize the study of chromosome architecture in many fields and at many different scales.

Methods

Drosophila embryo collection

Oregon-R w^{1118} fly stocks were maintained at room temperature with natural light/dark cycle and raised in standard cornmeal yeast medium. Following a pre-laying period of 16-18 hours, flyes were put in new cages so they can lay eggs during 1.5 hours on yeasted 0.4% acetic acid agar plates. Embryos were then incubated at 25 ^{0}C for an extra hour with 2,5 h of total developmental time. Embryos collection, dechorionation, fixation and devitellination were as described (Trcek et al. 2017). Embryos were stored in methanol at -20 ^{0}C until further use.

Oligopaint libraries

Oligopaint libraries were obtained from the Oligopaint public database (http://genetics.med.harvard.edu/oligopaints) and consisted of unique 42-mer sequences with homology to the genome. Probe density was around 10-15 probes per kb. We selected 22 genomic regions of interest (barcodes from now on) in the *sna* locus (2L:15244500..15630000), spanning a total of ~400 kb with an average distance between barcodes of 17 kb. For each barcode, we obtained seventy-five probes, covering between 4-6 kb. One of the barcodes was selected as the fiducial barcode for image registration and drift correction.

Each oligo in our template primary probe library contained 5 regions: (from 5' to 3') i) a 20-nucleotide (nt) forward universal priming region for library amplification, ii) a 30/32-nt readout region for binding of a fluorescent secondary probe unique for each barcode, iii) the 42-nt genome homology region for *in situ* hybridization to the target chromosomal DNA sequence, iv) a duplication of 30/32-nt readout region to allow for the binding of a second secondary probe and v) a 20-nt reverse universal

priming region. An oligo pool with all the oligonucleotides used in this study (~2000) was ordered from Twist Bioscience (San Francisco, USA). The 4-step procedure used to amplify the oligopaint probes was as described elsewhere (Wang et al. 2016). Briefly, it consists of a i) limited-cycle PCR, with pairs of PCR primers targeting the 20-nt forward and reverse priming regions. The reverse primer also contained an additional T7 promoter sequence to allow for ii) further amplification via T7 *in vitro* transcription, which were then iii) converted to single-stranded DNA oligo probes via reverse transcription. Finally, iv) the intermediate RNA products were removed with alkaline hydrolysis and DNA oligo probes were purified via column purification.

Secondary readout 32-mer fluorescently-labeled oligonucleotides (readout probes) were synthesized by Integrated DNA Technologies (IDT; Coralville, USA). We employed 22 unique-sequence oligos, 21 of which have a cleavable Alexa-647 attached to the oligo whereas the one used for fiducial barcodes had a non-cleavable Rhodamine fluorophore. The cleavable bond was a disulfide linkage that was removable with the mild reducing agent Tris(2-carboxyethyl)phosphine (TCEP), and allowed us to eliminate the fluorescence of a particular barcode from one cycle to the next (Moffitt et al. 2016).

See Supplementary Table 1 for the coordinates of all barcodes used. Sequences for secondary oligonucleotides and PCR primers are described in Supplementary Tables 2-3. The whole set of Oligopaints used are in Table 4.

RNA in situ hybridization coupled with tyramide signal amplification (TSA)

The *in situ* hybridization protocol for RNA detection was that of (Kosman et al. 2004) with minor modifications to TSA reaction parameters according to (Shpiz, Lavrov, and Kalmykova 2014). Snail probe was described in (Lagha et al. 2013) and was made

with digoxigenin conjugated haptens. The primary antibody used to detect *sna* probe was sheep anti-digoxigenin conjugated with POD (Sigma-Aldrich cat #11207733910) with 1:500 working dilution. Alexa-488 coupled to tyramide was used (Invitrogen cat#B40953).

Hybridization of primary oligopaint libraries

Unlabeled or RNA labeled embryos were resuspended by sequential dilutions of methanol with 0.1% V/V Tween-20 PBS (PBT). Next, embryos were RNAse treated during 2 h, permeabilized 1 h with 0.5% Triton in PBS and rinsed with sequential dilutions (20 min each) of Triton/pHM buffer to 100% pHM (pHM = 2X SSC, NaH_2PO_4 0.1M pH=7, 0.1% Tween-20, 50% formamide (v/v)). Then, 225 pmols of the barcode probes were diluted in 30 µL of FHB (FHB = 50% Formamide, 10% dextran sulfate, 2X SSC, Salmon Sperm DNA 0.5 mg ml^{-1}). Barcodes and embryos were preheated at 80 ^{o}C during 15 min. The supernatant of pHM buffer was completely removed from embryos and 30 µL of barcodes-containing solution were rapidly added. Mineral oil was added on top of the mix to avoid evaporation and the sealed tube was deposited in a water bath at 80°C. Immediately, the water bath was set to 37 ^{o}C and let cooling down overnight. The next day, oil was carefully removed and embryos were washed two times at 37 ^{o}C during 20 min with 50 % formamide, 2X SSC, 0.3 % CHAPS. Next, embryos were sequentially washed at 37 ^{o}C for 20 min with serial dilutions of formamide/PBT to 100% PBT. An additional (optional) crosslink step with PFA 4% was performed and embryos were washed and resuspended in PBS. For the fiducial barcode readout, hybridization was performed in the bench before mounting the sample into the flow chamber. The sample was incubated with Rhodamine-labeled readout probe in hybridization buffer for 30 min at room temperature. Next, the

sample was washed and kept in PBT. An additional fixation step could be performed as described before. Finally, embryos were stained with 0.5 µg ml^{-1} of DAPI for 20 min, washed with PBT and stored at 4 ^{0}C until imaging.

Robotic microscope setup

All experiments were performed on a home-made imaging setup built on a RAMM modular microscope system (Applied Scientific Instrumentation - USA). The RAMM module was equipped with a 60x Plan-Achromat water-immersion objective (NA=1.2, Nikon – Japan). The objective lens was mounted on a closed-loop piezoelectric stage (Nano-F100, Mad City Labs Inc. - USA) allowing for a fine control of the focus and the acquisition of z-stacks when imaging embryos. A two-axis translation stage was used to move the sample laterally and select embryos before each experiment (MS2000, Applied Scientific Instrumentation – USA). Four lasers with excitation wavelengths of 405 nm, 488 nm, 561 nm, and 641 nm were used for fluorescence imaging (OBIS-405/488/640 and Sapphire-LP-561, Coherent – USA). Laser beams were combined by a series of dichroic mirrors (LaserMUX™, Semrock – USA), individually controlled by an acousto-optic tunable filter (AOTFnC-400.650, AAopto-electronic – France) and focused onto the back-focal plane of the objective through one of the excitation ports of the RAMM. Excitation and emission wavelengths were separated using a four-band dichroic mirror (zt405/488/561/640rpc-UF2, Chroma – USA) and the fluorescence signal was further filtered using a four-band filter (zet405/488/561/640m, Chroma – USA) before being imaged on a sCMOS camera (ORCA Flash 4.0V3, Hamamatsu – Japan). The final pixel size was 100 nm. A home-made autofocus system was used to correct for axial drift in real-time and maintain the sample in focus while imaging. This was achieved

as follows. Along with a separate path, a 785 nm infrared laser beam (OBIS-785, Coherent – USA) was focused onto the back focal plane of the objective and reached the coverslip-sample interface in total internal reflection conditions. The position of the reflected beam was measured by a position-sensitive detector (OBP-A-4H, Newport – USA) and any variations in the objective-sample distance were corrected through the z-positioning piezo stage using a proportional-integral-differential feedback loop.

For sequential hybridizations, a fluidic system similar to the one described by (K. H. Chen et al. 2015) was designed. The sample was mounted in a FCS2 flow chamber (Bioptechs – USA). Buffers and probe handling were computer-controlled using a combination of three eight-way valves (HVXM 8-5, Hamilton – USA) and a negative pressure pump (MFCS-EZ, Fluigent – France). The flow rate was monitored in real-time using an online flow unit (FLU_L_D, Fluigent – France), allowing for a precise control of injected volumes.

All instruments, including camera, stages, lasers, pump, and valves were controlled using a custom-made software package developed in LabView 2015 (National Instrument – USA). This software controlled and synchronized multi-color 3D imaging and automated fluid handling.

Image registration with sequential rounds of hybridization

Embryos labeled with a primary oligopaint library (see above) were attached to a poly-L-lysine coated coverslip and mounted into the FCS2 flow chamber, connected to the fluidics system and secured to the translation stage (see microscope setup). The fluidics system had 21 tubes connected and distributed as follows: 1 tube with 50 mL of washing buffer (WB, 2×SSC, 40% v/v formamide), 1 tube with 50 mL of 2x

SSC, 1 tube with 20 mL of imaging buffer (IM, 1xPBS, 5 % w/v glucose, 0.5 mg/mL glucose oxidase and 0.05 mg/mL catalase), 1 tube with 50 mL of chemical bleaching buffer (CB, 2X SCC, 50 mM TCEP hydrochloride) and 17 tubes with 2.5 mL of each readout probe solution (25 nM readout probe, 2×SSC, 40% v/v formamide).

Embryos remained firmly attached when confronted with constant flow (~200 uL/min) for more than 72 hs, largely exceeding the total imaging time required for a single experiment (Figure 1SC). Following embryo selection, embryos were segmented into a mosaic of several fields of view (FOV of size 200 x 200 µm). First, bright field images were taken for all FOV. Next, DAPI and RNA staining were imaged together with fiducial barcodes by exciting at 405, 488 and 561 nm respectively. Fiducial barcodes hybridized to a Rhodamine-labeled readout probe before mounting the sample. Z-stacks of 15 µm with steps of 250 nm were acquired for all channels. Then, the robotic microscope controlled the sequential hybridization and imaging procedure (see Figure S1B). The flow chamber was initially flushed with 1.7 mL readout hybridization mixture over the span of 15 min to exchange buffers fully and ensure to saturate binding of readout probes. Next, the sample was washed with 2 mL of wash buffer for 18 min. Then 1.5 mL of 2X SSC were flushed during 15 min and finally 0.9 mL of imaging buffer was injected in 5 min. At this stage, flow was stopped, and ∼100 FOVs were imaged in two channels by exciting at 561 and 641 nm to image fiducial barcodes and readout probes, respectively (see Figure S1B). After imaging, the fluorescence of the readout probes was extinguished using chemical bleaching by flowing 2 mL of CB buffer for 15 min. The Rhodamine-labeled fiducial barcode was insensitive to chemical removal. In all cases, the flow speed varied between 0.1 and 0.25 mL/min. After chemical bleaching, the chamber was flushed with 2 mL of 2× SSC for 5 min and a new hybridization cycle started. A

standard experiment required between 30 and 40 h depending on the number of probes and number of imaged FOV.

All buffers were freshly prepared and filtered for each experiment. To avoid degradation by oxygen, the imaging buffer used for a single experiment was stored under a layer of mineral oil throughout the measurement. Imaging buffer was renewed every 12-15 hours.

Data processing and image analysis

First, images were deconvolved by Huygens Professional version 18.04 (Scientific Volume Imaging, The Netherlands, http://svi.nl), using the CMLE algorithm (SNR:20, 40 iterations) run with a custom-made script written in Tcl/Tk. All further analysis steps were performed using a homemade analysis pipeline developed using MATLAB Release 2017b (The MathWorks, Inc., Natick, United States). We corrected for x-y drift using the correlation-based alignment of whole images obtained for the fiducial barcode in every cycle for each embryo. After this initial global correction, fiducials were pre-segmented using an adaptive threshold and their positions fitted using a 3D Gaussian fitting algorithm. After this fitting procedure, a filtering step removing fiducial barcodes with sizes larger than the diffraction limit of light (~2.2 pixels for our microscope) was applied. Using the position of the selected fiducials from the first hybridization cycle (reference cycle), a local correlation-based alignment in 3D was performed by selecting cropped images centered in the fiducial for all cycles. This allowed for subpixel accuracy drift correction across the whole FOV. Next, barcodes were segmented for all hybridization cycles in batch processing mode using an optimized adaptive threshold. Positions of each barcode were determined by 3D Gaussian fitting of the segmented regions. These positions were corrected for

drift by using the closest fiducial barcode vector obtained from the previous analysis step. Nuclei were segmented from DAPI images by adaptive local thresholding and watershed filtering. RNA images were segmented by manually drawing polygons over the nuclei displaying a pattern of active transcription. This was used to assign an expression status for each DAPI-segmented cell. Then, barcodes were attributed to each cell by using the DAPI segmentation. The efficiency of labeling per cycle for all barcodes was 60-70 percent (Figure S1E). The barcode localizations for each cell were then clustered as follows. First, the mean number of localizations per readout code was found and used as a measure of the maximum number of clusters N (1 cluster for paired chromosomes, 2 clusters for unpaired chromosomes, etc). Then, K-means was used to separate barcodes positions into N clusters. Finally, pairwise distances and contact frequencies were calculated for each cluster in each cell.

All image processing was carried out on Linux terminals connected to a server running Linux Ubuntu 16.04 Xenial or CentOS 7, with 32 CPU processors, two GeForce GTX 1080Ti GPU cards, and 128GB of RAM.

Multiscale correlation of Hi-M mean distance maps

To compare Hi-M matrices at different scales, we did the following steps. First, we convolved maps with a Gaussian kernel of size s (standard deviation). Then, we calculated the correlation between maps and repeated this process for different values of s, ranging from 0.1 to 5. These values correspond to approximate genomic sizes ranging from 5 to 150 kb. As a control, we simulated random matrices with the same sizes and intensity ranges as the experimental matrices and repeated the same procedure. This process was repeated for 200 random matrices and the average correlation curves are shown in Figure 2B.

Precision of the method and absolute contact probability

The mean localization accuracy after drift correction was 43 ± 21 nm in xy and 51 ± 58 nm in z (Figure S1C). This was obtained by measuring the distance between fiducial barcodes after applying the correction obtained from the previously described image correlation method. To further verify the precision of co-localization, a single locus was simultaneously labeled with encoding probes bearing binding sites for two distinct readout probes. After image registration, two sequential hybridization cycles with readout probes targeting the selected loci were performed. The co-localization precision after drift correction was of 83 ± 60 nm in xyz (Figure S1D). To further challenge the quality of drift correction and co-localization, a similar control experiment was performed but separating the readout hybridization cycles by 10 additional cycles and by letting the sample mounted in the microscope rest more than 24 hs. In these conditions, drift correction accuracy and precision of colocalization were equivalent to the previous control, ensuring that our internal marquer drift correction was unaffected by the set-up or sample stability during long acquisitions. As previously described (Cattoni et al. 2017), we estimated the absolute contact probability between two loci by integrating the total number of observations that are below a threshold that represents 100% of co-localizations of the double-labeled control (120 nm).

Hi-C and Chip-Seq data processing

Raw Hi-C sequencing data were processed using the scHiC2 pipeline (Nagano et al. 2017). Construction of expected models and Hi-C contact scoring was performed using the 'shaman' R package (https://bitbucket.org/tanaylab/shaman, (Cohen,

Abraham, and Ober 2017). Raw ChIPseq sequencing data were mapped to the dm3 reference genome using the bowtie.2 algorithm. Linear read density profiles at 10bp resolution where produced using MACS 1.4 (Zhang et al. 2008) after merging replicates. RNAseq RPM (reads per million) profiles where produced by aligning raw, paired-end, sequencing reads to the dm3 reference genome (BDGP R5/dm3 UCSC gene annotation) using STAR (Dobin et al, 2013) with ‘unstranded’ output.

We interpolated Hi-C matrices to make comparisons with Hi-M maps. For this, we extracted the contact frequencies at the genomic positions at which barcodes were located to construct an interpolated Hi-C map. Interpolated and full Hi-C maps displayed very similar features (Figures S1F, S3A).

Code availability

Computer code is available upon request.

Data availability

The data that support the findings of this study are available from the corresponding author upon request. Hi-C and Chip-seq data source and reference are in Table 5.

Acknowledgments

This project has received funding from the European Research Council (ERC) under the European Union's Horizon 2020 research and innovation programme (Grant Agreement No 724429). This work also benefited from support by the Labex EpiGenMed, an «Investments for the future» program, reference ANR-10-LABX-12-01. We acknowledge the France-BioImaging infrastructure supported by the French National Research Agency (ANR-10-INBS-04, «Investments for the future»). This work was also supported by the ERC SyncDev starting grant to M.L.

Authors contribution

A.M.C.G., M.L. and M.N. designed experiments. A.M.C.G., D.I.C., S.E., J.G. and O.M. conducted research. J.B.F. designed and built microscopy setup and acquisition software. M.N. developed software for image analysis. A.M.C.G., J.G., and M.N. analyzed data. A.M.C.G. and M.N. designed oligopaint probes. J.G and O.M. performed fly handling. C.H. synthesized and purified oligopaints libraries. Y.O., G-L. P. and G.C. performed Hi-C experiments and analysis. A.M.C.G., D.I.C, and M.N. wrote the manuscript. All the authors reviewed and commented on the data.

Competing financial interests

The authors declare no competing financial interests.

References

Alberga, A., J. L. Boulay, E. Kempe, C. Dennefeld, and M. Haenlin. 1991. “The Snail Gene Required for Mesoderm Formation in Drosophila Is Expressed Dynamically in Derivatives of All Three Germ Layers.” *Development* 111 (4): 983–92.

Ashraf, S. I., X. Hu, J. Roote, and Y. T. Ip. 1999. “The Mesoderm Determinant Snail Collaborates with Related Zinc-Finger Proteins to Control Drosophila Neurogenesis.” *The EMBO Journal* 18 (22): 6426–38.

Beliveau, Brian J., Alistair N. Boettiger, Maier S. Avendaño, Ralf Jungmann, Ruth B. McCole, Eric F. Joyce, Caroline Kim-Kiselak, et al. 2015. “Single-Molecule Super-Resolution Imaging of Chromosomes and in Situ Haplotype Visualization Using Oligopaint FISH Probes.” *Nature Communications* 6 (May): 7147.

Beliveau, Brian J., Eric F. Joyce, Nicholas Apostolopoulos, Feyza Yilmaz, Chamith Y. Fonseka, Ruth B. McCole, Yiming Chang, et al. 2012. “Versatile Design and Synthesis Platform for Visualizing Genomes with Oligopaint FISH Probes.” *Proceedings of the National Academy of Sciences of the United States of America* 109 (52): 21301–6.

Blythe, Shelby A., and Eric F. Wieschaus. 2016. “Establishment and Maintenance of Heritable Chromatin Structure during Early Drosophila Embryogenesis.” *eLife* 5. https://doi.org/10.7554/elife.20148.

Boettiger, Alistair N., Bogdan Bintu, Jeffrey R. Moffitt, Siyuan Wang, Brian J. Beliveau, Geoffrey Fudenberg, Maxim Imakaev, Leonid A. Mirny, Chao-Ting Wu, and Xiaowei Zhuang. 2016. “Super-Resolution Imaging Reveals Distinct Chromatin Folding for Different Epigenetic States.” *Nature* 529 (7586): 418–22.

Cattoni, Diego I., Andrés M. Cardozo Gizzi, Mariya Georgieva, Marco Di Stefano, Alessandro Valeri, Delphine Chamousset, Christophe Houbron, et al. 2017. “Single-Cell Absolute Contact Probability Detection Reveals Chromosomes Are Organized by Multiple Low-Frequency yet Specific Interactions.” *Nature Communications* 8 (1): 1753.

Chen, Kai, Jeff Johnston, Wanqing Shao, Samuel Meier, Cynthia Staber, and Julia Zeitlinger. 2013. “A Global Change in RNA Polymerase II Pausing during the Drosophila Midblastula Transition.” *eLife* 2 (August): e00861.

Chen, K. H., A. N. Boettiger, J. R. Moffitt, S. Wang, and X. Zhuang. 2015. “RNA

Imaging. Spatially Resolved, Highly Multiplexed RNA Profiling in Single Cells. Science. 348: aaa6090.”

Chen, Kok Hao, Alistair N. Boettiger, Jeffrey R. Moffitt, Siyuan Wang, and Xiaowei Zhuang. 2015. “RNA Imaging. Spatially Resolved, Highly Multiplexed RNA Profiling in Single Cells.” *Science* 348 (6233): aaa6090.

Cohen, Edward A. K., Anish V. Abraham, and Raimund J. Ober. 2017. “Resolution Limit of Image Analysis Algorithms.” https://doi.org/10.1101/240531.

Cruz-Molina, Sara, Patricia Respuela, Christina Tebartz, Petros Kolovos, Milos Nikolic, Raquel Fueyo, Wilfred F. J. van Ijcken, et al. 2017. “PRC2 Facilitates the Regulatory Topology Required for Poised Enhancer Function during Pluripotent Stem Cell Differentiation.” *Cell Stem Cell* 20 (5): 689–705.e9.

Dixon, Jesse R., David U. Gorkin, and Bing Ren. 2016. “Chromatin Domains: The Unit of Chromosome Organization.” *Molecular Cell* 62 (5): 668–80.

Dixon, Jesse R., Inkyung Jung, Siddarth Selvaraj, Yin Shen, Jessica E. Antosiewicz-Bourget, Ah Young Lee, Zhen Ye, et al. 2015. “Chromatin Architecture Reorganization during Stem Cell Differentiation.” *Nature* 518 (7539): 331–36.

Dixon, Jesse R., Siddarth Selvaraj, Feng Yue, Audrey Kim, Yan Li, Yin Shen, Ming Hu, Jun S. Liu, and Bing Ren. 2012. “Topological Domains in Mammalian Genomes Identified by Analysis of Chromatin Interactions.” *Nature* 485 (7398): 376–80.

Eng, Chee-Huat Linus, Sheel Shah, Julian Thomassie, and Long Cai. 2017. “Profiling the Transcriptome with RNA SPOTs.” *Nature Methods* 14 (12): 1153–55.

Flyamer, Ilya M., Johanna Gassler, Maxim Imakaev, Hugo B. Brandão, Sergey V. Ulianov, Nezar Abdennur, Sergey V. Razin, Leonid A. Mirny, and Kikuë Tachibana-Konwalski. 2017. “Single-Nucleus Hi-C Reveals Unique Chromatin Reorganization at Oocyte-to-Zygote Transition.” *Nature* 544 (7648): 110–14.

Fung, J. C., W. F. Marshall, A. Dernburg, D. A. Agard, and J. W. Sedat. 1998. “Homologous Chromosome Pairing in Drosophila Melanogaster Proceeds through Multiple Independent Initiations.” *The Journal of Cell Biology* 141 (1): 5–20.

Hemavathy, Kirugaval, Xiaodi Hu, Shovon I. Ashraf, Stephen J. Small, and Y. Tony Ip. 2004. “The Repressor Function of Snail Is Required for Drosophila Gastrulation and Is Not Replaceable by Escargot or Worniu.” *Developmental Biology* 269 (2): 411–20.

Hnisz, Denes, Abraham S. Weintraub, Daniel S. Day, Anne-Laure Valton, Rasmus O. Bak, Charles H. Li, Johanna Goldmann, et al. 2016. “Activation of Proto-Oncogenes by Disruption of Chromosome Neighborhoods.” *Science* 351 (6280): 1454–58.

Hug, Clemens B., Alexis G. Grimaldi, Kai Kruse, and Juan M. Vaquerizas. 2017. “Chromatin Architecture Emerges during Zygotic Genome Activation Independent of Transcription.” *Cell* 169 (2): 216–28.e19.

Joyce, Eric F., Benjamin R. Williams, Tiao Xie, and C. -ting Wu. 2012. “Identification of Genes That Promote or Antagonize Somatic Homolog Pairing Using a High-Throughput FISH–Based Screen.” *PLoS Genetics* 8 (5): e1002667.

Korzelius, Jerome, Svenja K. Naumann, Mariano A. Loza-Coll, Jessica Sk Chan, Devanjali Dutta, Jessica Oberheim, Christine Gläßer, et al. 2014. “Escargot Maintains Stemness and Suppresses Differentiation in Drosophila Intestinal Stem Cells.” *The EMBO Journal* 33 (24): 2967–82.

Kosman, Dave, Claudia M. Mizutani, Derek Lemons, W. Gregory Cox, William McGinnis, and Ethan Bier. 2004. “Multiplex Detection of RNA Expression in Drosophila Embryos.” *Science* 305 (5685): 846.

Lagha, Mounia, Jacques P. Bothma, Emilia Esposito, Samuel Ng, Laura Stefanik, Chiahao Tsui, Jeffrey Johnston, et al. 2013. “Paused Pol II Coordinates Tissue Morphogenesis in the Drosophila Embryo.” *Cell* 153 (5): 976–87.

Lieberman-Aiden, Erez, Nynke L. van Berkum, Louise Williams, Maxim Imakaev, Tobias Ragoczy, Agnes Telling, Ido Amit, et al. 2009. “Comprehensive Mapping of Long-Range Interactions Reveals Folding Principles of the Human Genome.” *Science* 326 (5950): 289–93.

Moffitt, Jeffrey R., Junjie Hao, Guiping Wang, Kok Hao Chen, Hazen P. Babcock, and Xiaowei Zhuang. 2016. “High-Throughput Single-Cell Gene-Expression Profiling with Multiplexed Error-Robust Fluorescence in Situ Hybridization.” *Proceedings of the National Academy of Sciences of the United States of America* 113 (39): 11046–51.

Nagano, Takashi, Yaniv Lubling, Csilla Várnai, Carmel Dudley, Wing Leung, Yael Baran, Netta Mendelson Cohen, Steven Wingett, Peter Fraser, and Amos Tanay. 2017. “Cell-Cycle Dynamics of Chromosomal Organization at Single-Cell Resolution.” *Nature* 547 (7661): 61–67.

Naumova, Natalia, Maxim Imakaev, Geoffrey Fudenberg, Ye Zhan, Bryan R. Lajoie,

Leonid A. Mirny, and Job Dekker. 2013. “Organization of the Mitotic Chromosome.” *Science* 342 (6161): 948–53.

Nègre, Nicolas, Christopher D. Brown, Parantu K. Shah, Pouya Kheradpour, Carolyn A. Morrison, Jorja G. Henikoff, Xin Feng, et al. 2010. “A Comprehensive Map of Insulator Elements for the Drosophila Genome.” *PLoS Genetics* 6 (1): e1000814.

Nishino, Yoshinori, Mikhail Eltsov, Yasumasa Joti, Kazuki Ito, Hideaki Takata, Yukio Takahashi, Saera Hihara, et al. 2012. “Human Mitotic Chromosomes Consist Predominantly of Irregularly Folded Nucleosome Fibres without a 30-Nm Chromatin Structure.” *The EMBO Journal* 31 (7): 1644–53.

Nora, Elphège P., Bryan R. Lajoie, Edda G. Schulz, Luca Giorgetti, Ikuhiro Okamoto, Nicolas Servant, Tristan Piolot, et al. 2012. “Spatial Partitioning of the Regulatory Landscape of the X-Inactivation Centre.” *Nature* 485 (7398): 381–85.

Ogiyama, Yuki, Bernd Schuettengruber, Giorgio L. Papadopoulos, Jia-Ming Chang, and Giacomo Cavalli. 2018. “Polycomb-Dependent Chromatin Looping Contributes to Gene Silencing during Drosophila Development.” *Molecular Cell* 71 (1): 73–88.e5.

Phanstiel, Douglas H., Kevin Van Bortle, Damek Spacek, Gaelen T. Hess, Muhammad Saad Shamim, Ido Machol, Michael I. Love, Erez Lieberman Aiden, Michael C. Bassik, and Michael P. Snyder. 2017. “Static and Dynamic DNA Loops Form AP-1-Bound Activation Hubs during Macrophage Development.” *Molecular Cell* 67 (6): 1037–48.e6.

Sexton, Tom, Eitan Yaffe, Ephraim Kenigsberg, Fr d. Ric Bantignies, Benjamin Leblanc, Michael Hoichman, Hugues Parrinello, Amos Tanay, and Giacomo Cavalli. 2012. “Three-Dimensional Folding and Functional Organization Principles of the Drosophila Genome.” *Cell* 148 (3): 458–72.

Shah, Sheel, Yodai Takei, Wen Zhou, Eric Lubeck, Jina Yun, Chee-Huat Linus Eng, Noushin Koulena, et al. 2018. “Dynamics and Spatial Genomics of the Nascent Transcriptome by Intron seqFISH.” *Cell* 174 (2): 363–76.e16.

Shpiz, Sergey, Sergey Lavrov, and Alla Kalmykova. 2014. “Combined RNA/DNA Fluorescence in Situ Hybridization on Whole-Mount Drosophila Ovaries.” *Methods in Molecular Biology* 1093: 161–69.

Spielmann, Malte, Darío G. Lupiáñez, and Stefan Mundlos. 2018. “Structural Variation in the 3D Genome.” *Nature Reviews. Genetics* 19 (7): 453–67.

Stadhouders, Ralph, Enrique Vidal, François Serra, Bruno Di Stefano, François Le

Dily, Javier Quilez, Antonio Gomez, et al. 2018. “Transcription Factors Orchestrate Dynamic Interplay between Genome Topology and Gene Regulation during Cell Reprogramming.” *Nature Genetics* 50 (2): 238–49.

Stevens, Tim J., David Lando, Srinjan Basu, Liam P. Atkinson, Yang Cao, Steven F. Lee, Martin Leeb, et al. 2017. “3D Structures of Individual Mammalian Genomes Studied by Single-Cell Hi-C.” *Nature* 544 (7648): 59–64.

Szabo, Quentin, Daniel Jost, Jia-Ming Chang, Diego I. Cattoni, Giorgio L. Papadopoulos, Boyan Bonev, Tom Sexton, et al. 2018. “TADs Are 3D Structural Units of Higher-Order Chromosome Organization in.” *Science Advances* 4 (2): eaar8082.

Trcek, Tatjana, Timothée Lionnet, Hari Shroff, and Ruth Lehmann. 2017. “mRNA Quantification Using Single-Molecule FISH in Drosophila Embryos.” *Nature Protocols* 12 (7): 1326–48.

Wang, Siyuan, Jun-Han Su, Brian J. Beliveau, Bogdan Bintu, Jeffrey R. Moffitt, Chao-Ting Wu, and Xiaowei Zhuang. 2016. “Spatial Organization of Chromatin Domains and Compartments in Single Chromosomes.” *Science* 353 (6299): 598–602.

Zhang, Yong, Tao Liu, Clifford A. Meyer, Jérôme Eeckhoute, David S. Johnson, Bradley E. Bernstein, Chad Nusbaum, et al. 2008. “Model-Based Analysis of ChIP-Seq (MACS).” *Genome Biology* 9 (9): R137.

Figure legends

Fig 1. Hi-M enables exploration of chromosome structure in single cells within intact organisms with high genomic coverage and high spatial resolution.

A. Schematic representations of an example locus and the labeling strategy are shown. TADs are depicted as blue/green triangles, genes as arrows, insulators as red triangles. Barcodes are indicated as rectangles with a color code following their genomic location. Inset: each barcode is composed of multiple short oligonucleotides with a genome homology region (black), a region for secondary oligo binding (green) and a fluorescent readout probe (black and red).

B. Schematic representation of the Hi-M setup. A robotic multi-color, 3D widefield imaging system was coupled to an automatic fluid-handling device (see main text and Methods). Multiplexed barcode imaging is achieved by injecting readout probes sequentially (depicted as colored rectangles). Within the microfluidics chamber, *Drosophila* embryos are attached to a poly-lysine treated coverslip.

C. Acquisition and analysis Hi-M imaging pipeline (see Figures S1A-C for more details). An entire embryo is shown where each nuclei is represented by a different color (left). Image registration phase: each nuclei within a field-of-view is segmented based on DAPI staining (left panel). Next, masks were classified according to RNA expression levels as expressing (green) or not expressing (black, middle panel). Fiducial barcodes are imaged, segmented and localized (right panel). Multiplexed barcode imaging phase: readout probes are sequentially injected, imaged, segmented and localized. Reconstruction phase: after drift correction, the 3D position of all barcodes were retrieved for

each nuclei in the embryo.

D. Hi-C map of nc 14 Drosophila embryos for the region 2L:15.250-15.650 Mb indicating normalized contact probability with a scale going from white (low) to blue (high). TADs detected by Hi-C (TAD-1 and TAD-2) are delineated with blue and green dotted lines, respectively. Lower panels: genes, RNA-Seq from embryos 2-4 hours of development, Chip-seq from Phospho RNA pol II (S5) from nc 14 embryos and Chip-Seq against CP190. Genomic positions of barcodes are represented as in panel A.

E-F. Mean physical distance (C) and absolute contact probability (D) *vs.* genomic distance from Hi-M (blue circles). Black filled circles are data points from our previous study, where we performed pairwise measurements in *Drosophila* embryo cells in a different locus using 3D-structured illumination microscopy (Cattoni et al. 2017). Solid red lines depict a power-law fit with the scaling exponents $\beta = 0.23 \pm 0.02$ for panel E and $\alpha = -0.4 \pm 0.02$ for panel F.

G. Hi-M map and interpolated Hi-C matrix from nc 14 wild-type embryos spanning the ~400 kb region encompassing *sna* and *esg*. Barcodes are represented as in panel A. *esg* and *sna* are indicated with magenta and red lines, respectively. Features observed in Hi-C at the interpolated resolution and at 5 kb resolution are equivalent (Figure S1H). Relative (Hi-C) and absolute (Hi-M) contact frequencies are color-coded according to scale bar. A good correlation between Hi-M replicates was found (Pearson correlation = 0.92, Figure S1G). N = 6643.

H. Normalized Hi-M contact maps from nc 14 wild-type *Drosophila* embryos. Normalization is achieved by dividing observed *vs* expected contact frequencies for equivalent genomic distance. The expected contact frequency

is obtained from fit in panel F. Color scale on the right indicates fold enrichment in log scale (positive, blue; negative, red; white, equal). Green arrows indicate chromosomal regions with contact frequencies lower than expected. TADs detected by Hi-C are shown with dotted black lines. Barcodes are represented as in panel A.

I. Normalized mean physical distance map from nc 14 wild-type *Drosophila* embryos. Normalization is achieved by subtracting observed and expected distances. The expected distance was obtained from the fit in panel E. Color scale indicates distances lower (magenta) or higher (cyan) than expected. Normalised distances are in nm. Red arrow indicate regions displaying distances higher than expected. TADs detected by Hi-C are shown with dotted black lines. Barcodes are represented as in panel A.

Fig 2. Chromosome architecture in unpaired and paired homologous chromosomes.

A. Hi-M normalized distance maps from paired (top panel) or unpaired (lower panel) homologous chromosomes. Barcodes are represented as in Fig 1A. Schematic representation indicate paired/un-paired homologous chromosomes (top-right and bottom-right panels). N= 1564 (paired), N=5052 (unpaired).

B. Multi-scale correlation of Hi-M normalized distance maps for paired and unpaired chromosomes. Blue circles represent the correlation of maps at different resolutions. Red circles represent the correlation between randomized matrices as a function of resolution. Insets show interpolated

unpaired Hi-M maps at different resolutions, with color codes as in Figure 1I.

C. Correlation of Hi-M normalized mean pairwise distances between paired and unpaired homologous chromosomes. Pearson correlation coefficient = 0.91.

Fig 3. In situ, single-cell exploration of chromosome conformation during the cell cycle and development.

A,E and I. Top, schematic representation of an embryo undergoing mitosis (A), nc 9-13 (pre-MBT) (E) and nc 14 (MBT) (I). Bottom, DAPI image of a representative embryo of the corresponding stage.

B,F and J. Hi-M map (upper right triangle) and interpolated Hi-C matrix (lower left triangle) from embryos undergoing mitosis (B), nc 9-13 (pre-MBT) (F) and nc 14 (MBT) (J). Barcodes are represented as in Figure 1A. Features observed in Hi-C at the interpolated resolution and at 5 kb resolution are equivalent (Figure S3A). Relative (Hi-C) and absolute (Hi-M) contact frequencies are color-coded according to scale bar. N= 1430 (mitosis), N=2933 (nc12-13), N=6643 (nc14).

C,G and K. Normalized Hi-M contact maps from embryos undergoing mitosis (C), nc 9-13 (pre-MBT) (G) and nc 14 (MBT) (K). Color scale on top as in Figure 1H. TADs assigned by Hi-C are shown with dotted black lines. Barcodes are represented as in Figure 1A.

D,H and L. Normalized mean physical distance maps from embryos undergoing mitosis (D), nc 9-13 (pre-MBT) (H) and nc 14 (MBT) (L). Color scale on top as in Figure 1I. TADs observed in nc 14 are delineated with dotted blue lines. Barcodes are represented as in Figure 1A. Schematic representations for each developmental state are shown below matrices. Blue and green represent the chromatin fiber in each of the two TADs detected by Hi-C.

Fig. 4. Simultaneous detection of chromosome organization and transcription by Hi-M.

A. Single-cell RNA expression detection. Top: scheme depicting the Hi-M experimental design. Bottom left: Representative full embryo *sna* RNA image obtained from the image registration step. Bottom right: result of nuclei segmentation and RNA state assignation for the full embryo. Nuclei expressing *sna* are in green whereas nuclei not expressing *sna* appear in black.

B-C. Hi-M absolute contact matrices for nuclei expressing (C) or not (B) expressing *sna*. Absolute contact frequency is color-coded according to scale bar. Barcodes are represented as in Figure 1D. N=4402 (off) and N=2265 (on).

D-E. Normalized Hi-M distance maps for nuclei expressing (E) or not (D) expressing *sna*. Color scale indicates distances shorter (magenta) or higher (cyan) than expected (scale in nm). Solid lines represent the positions of *sna* and *esg*. Barcodes are represented as colored as in Figure 1A. On the bottom, schematic representations of TAD organization in transcriptionally *on/off* nuclei are shown. TAD-1 is represented in blue and TAD-2 in green.

Supplementary figure legends

Figure S1

A. Schematic representation of barcodes and sequential hybridization steps. The primary DNA hybridization using an oligopaint library was made at the bench. Next, hybridization with the fiducial barcode readout (insensitive to chemical bleaching) was performed also at the bench and was followed by a crosslinking step. Embryos were then immobilized within a microfluidics device. Each sequential hybridization cycle comprised the injection of a readout probe, incubation, imaging and chemical cleavage of the fluorophore from the readout probe.

B. Schematic representation of Hi-M acquisition pipeline. A first image registration phase comprised the imaging of DAPI-stained nuclei, of RNA probes, and of fiducial barcodes. Sequential hybridization/imaging cycles were performed within the robotic microscope and comprised the steps described schematically in the figure.

C. Embryo stability at the beginning and end of a 72h Hi-M acquisition. Embryos were attached to a poly-L-lysine-coated coverslip and mounted onto the microfluidics chamber. A representative field-of-view displaying a region of an embryo in the fiducial barcode channel is shown. Colors represent fluorescence intensity signal of fiducial barcode at 0h (red) and 72 h (green). Images were drift corrected using the protocol described in Methods. Inset displays a magnification of the selected area.

D. Left panel, boxplot of the residual error in xyz between fiducial barcodes after the global and local drift correction. The global correction was obtained by cross-correlation of fiducial barcode images at different cycles. An improved

local correction is obtained by: (1) segmenting fiducial barcodes in the first cycle; (2) subvolumes of size 20x20x60 pixels centered at each segmented object are extracted for the first cycle; (3) subvolumes are extracted for other cycles. Here the center of the subvolume is interpolated by using the localization of the fiducial mark in the first cycle and the global correction for each cycle obtained by image cross-correlation; (4) each subvolume *i* in cycle *j* is cross-correlated with subvolume *i* in cycle 1 to obtain a local correction vector specific for fiducial barcode *i*. A final correction vector for each segmented fiducial barcode and for each cycle is obtained by adding the global and local correction vectors. Middle panel: Examples of subvolumes for 3 fiducial barcodes (rows) are shown for all cycles. A typical field-of-view contains hundreds of fiducial barcodes. Right panel, boxplot of the residual error after the global and local correction in xy and z directions. Median values: 42 nm (xy) and 51 nm (z).

E. To validate the drift correction method, we sequentially labeled and imaged a single barcode using two readout probes. Then, we calculated the distances the residual errors after global and local drift corrections and plotted them as a boxplot. The remaining mean xyz residual error was smaller than 90 nm.

F. Mean representative labeling efficiencies for each imaging cycle. Labeling efficiency is defined as the number of nuclei having at least one detected barcode in the corresponding cycle over the total number of nuclei.

G. Comparison between interpolated (upper triangle) and full resolution (5kb) Hi-C normalized maps (bottom triangle) for nc 14 embryos.

H. Correlation between Hi-M contact probability and Hi-C normalized counts. Pearson correlation coefficient = 0.91.

I. Correlation of Hi-M mean pairwise distances for two independent replicates. Pearson correlation coefficient = 0.92.

Figure S2

A. Distribution in the number of spots detected per barcode in a representative nc 14 embryo. Each subplot represents a different barcode. Pairing was similar for all barcodes (>70%), consistent with previous studies (Fung et al. 1998; Cattoni et al. 2017). For representation purposes, only nuclei with up to 3 spots/barcode/nucleus are shown. The nuclei with four or more spots/barcode/ nucleus was <3%.

B. Right panels: Hi-M absolute contact probability maps for paired and unpaired chromosomes. Left panels: schemes of paired and unpaired chromosomes.

C. Hi-M normalized contact probability maps of paired (upper panel) and unpaired (lower panel) chromosomes. Dashed black boxes represent TADs detected by Hi-C.

Figure S3

A-C. Comparison between interpolated (upper triangles) and full resolution (5 kb) Hi-C normalized maps (bottom triangles) for embryos in mitosis (A) nc 9-13 (B) and nc 14 (C).

D. H-M absolute contact probabilities *vs.* genomic distances for embryos in mitosis (left panel), nc 9-13 (middle panel) and nc 14 (right panel). Solid red lines are power-law fits with the scaling exponent indicated in the insets.

Figure S4

A. Full resolution (5kb) Hi-C map for nc 14 embryos. Relative contact frequency is color-coded according to scale bar (log scale). Black dotted circle indicates the position of the *sna-esg* loop. The positions of *esg* and *sna* are indicated with magenta and red lines, respectively. Top panel: schematic representation of the loop between *esg* and *sna*. Right panel displays: genes, Chip-Seq data for Zelda in nc 14, Chip-Seq for GAGA-factor (GAF) in stage 4-8, Chip-Seq of H3K27me3 in nc 14, Chip-seq for polycomb and Ph (Polycomb group proteins) in nc 14 and stage 12, respectively.

B. Normalized Hi-M distance maps for nuclei in nc 14 for *sna* inactive (left panels) and *sna* active nuclei (right panels). Raw maps are shown in the upper panels and gaussian filtered panels are displayed in the lower panels. Barcodes are shown below.

Figure 1

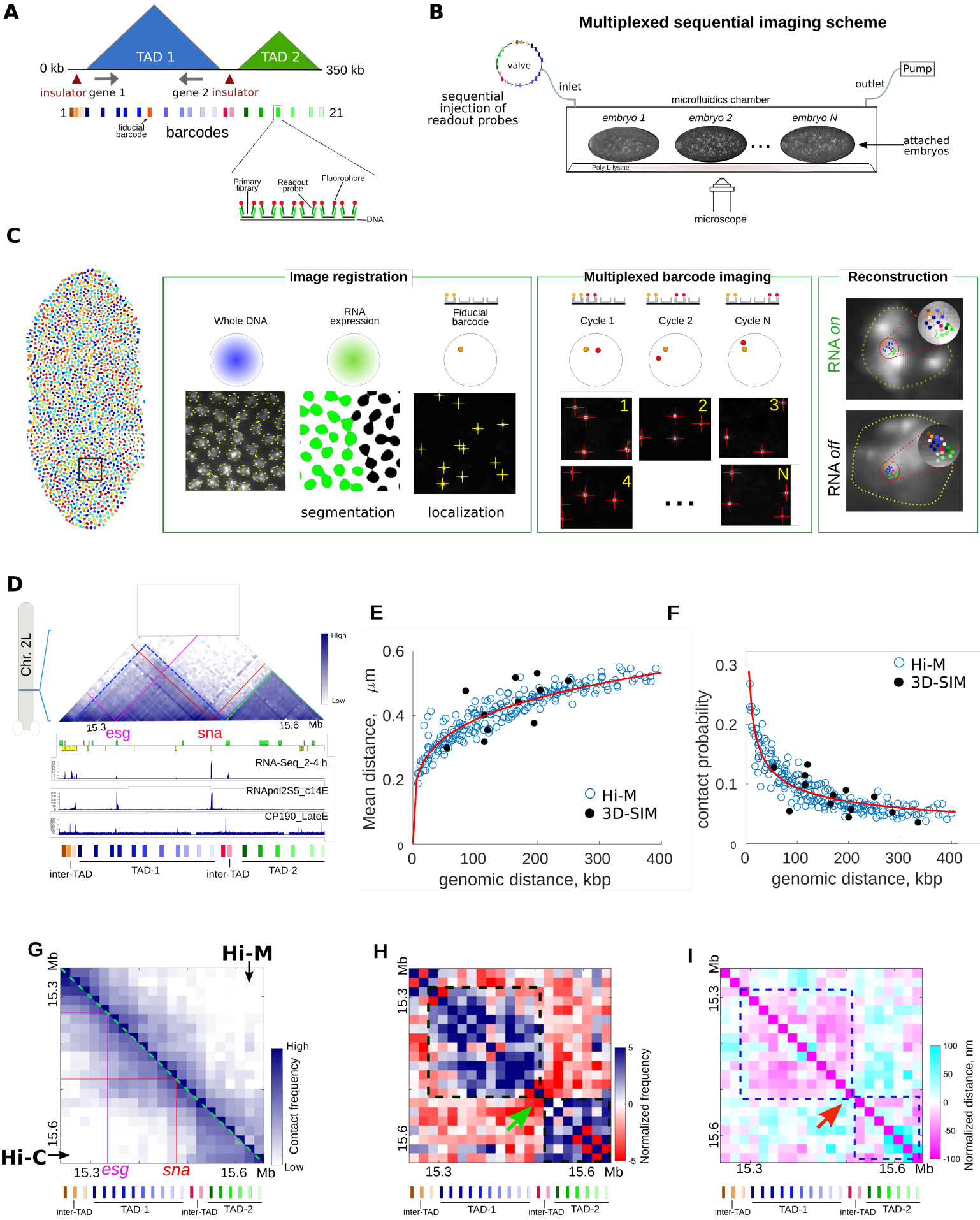
A
TAD 1
TAD 2
0 kb
350 kb
insulator
gene 1
gene 2
insulator
1
21
fiducial barcode
barcodes
Primary library
Readout probe
Fluorophore
DNA
B
Multiplexed sequential imaging scheme
valve
inlet
sequential injection of readout probes
microfluidics chamber
outlet
Pump
embryo 1
embryo 2
embryo N
attached embryos
Poly-L-lysine
microscope
C
Image registration
Whole DNA
RNA expression
Fiducial barcode
segmentation
localization
Multiplexed barcode imaging
Cycle 1
Cycle 2
Cycle N
Reconstruction
RNA on
RNA off
D
Chr. 2L
High
Low
15.3
esg
sna
15.6
Mb
RNA-Seq_2-4 h
RNApol2S5_c14E
CP190_LateE
inter-TAD
TAD-1
inter-TAD
TAD-2
E
Mean distance, μm
genomic distance, kbp
Hi-M
3D-SIM
F
contact probability
genomic distance, kbp
Hi-M
3D-SIM
G
Hi-M
Hi-C
Mb
15.3
15.6
High
Low
Contact frequency
esg
sna
inter-TAD
TAD-1
inter-TAD
TAD-2
H
Normalized frequency
I
Normalized distance, nm

Figure 2

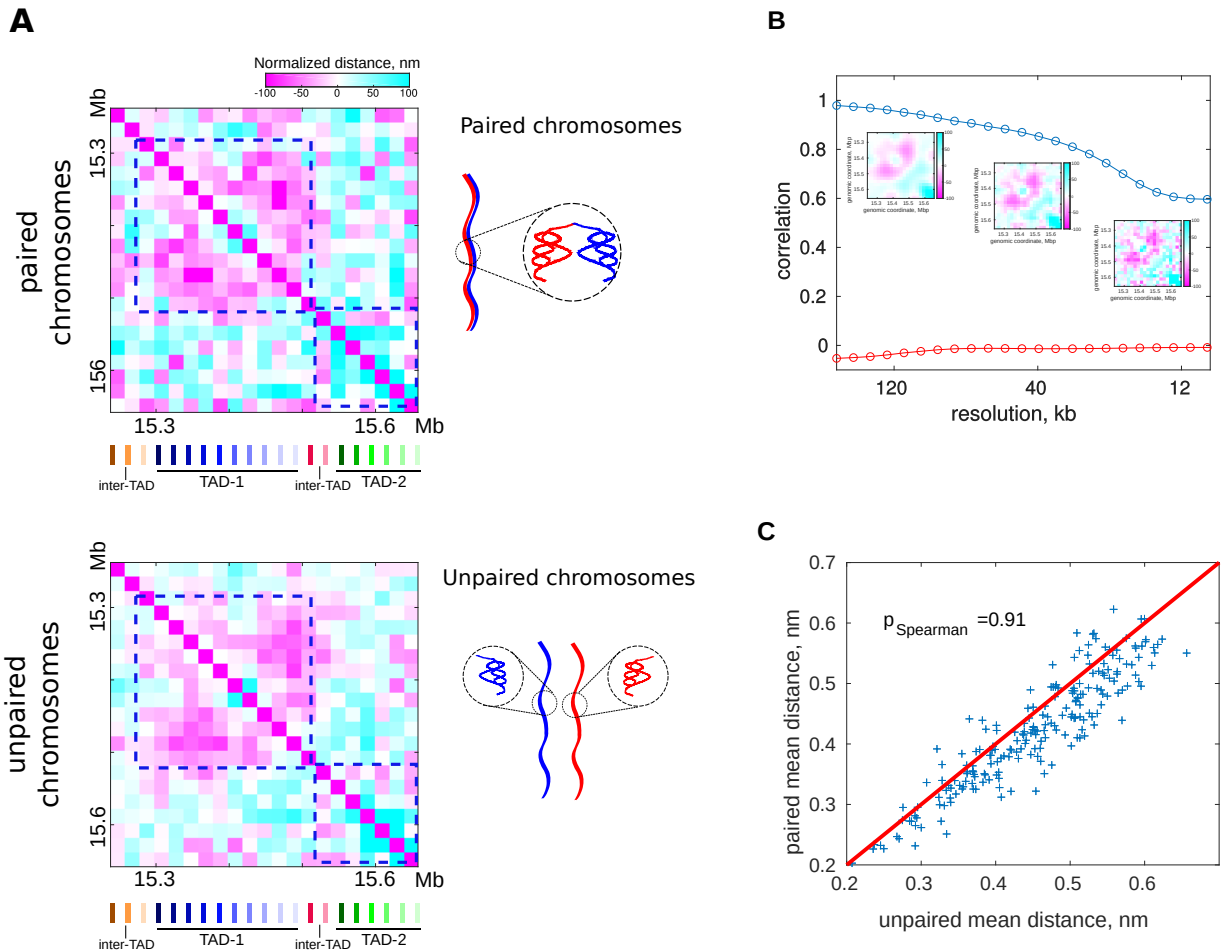
A
Normalized distance, nm
-100 -50 0 50 100
paired chromosomes
Mb
15.3
156
15.3
15.6 Mb
inter-TAD
TAD-1
inter-TAD
TAD-2
Paired chromosomes
unpaired chromosomes
Mb
15.3
15.6
15.3
15.6 Mb
inter-TAD
TAD-1
inter-TAD
TAD-2
Unpaired chromosomes
B
correlation
1
0.8
0.6
0.4
0.2
0
120
40
12
resolution, kb
C
paired mean distance, nm
unpaired mean distance, nm
0.7
0.6
0.5
0.4
0.3
0.2
0.2
0.3
0.4
0.5
0.6
p Spearman =0.91

Figure 3

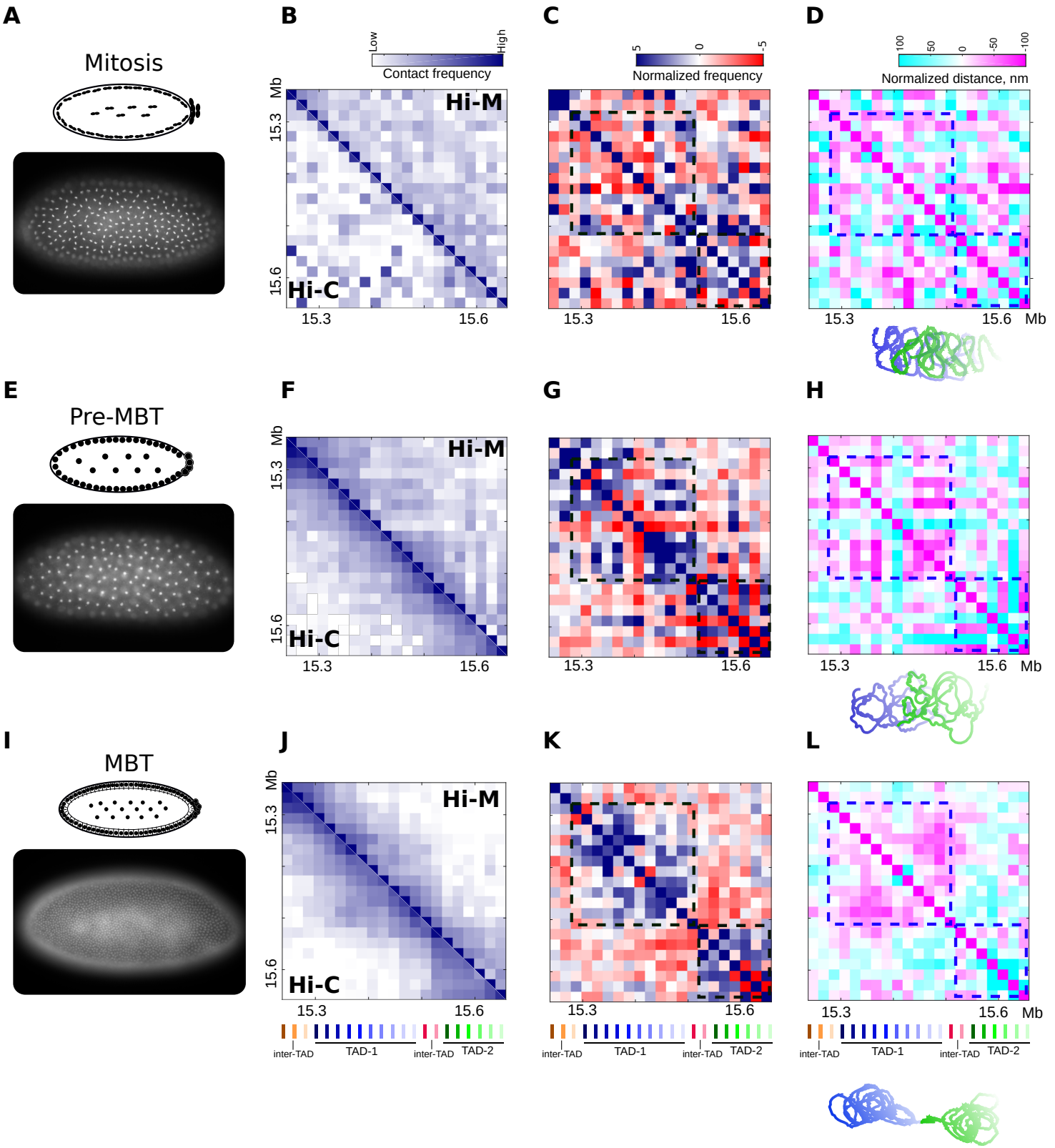
A
Mitosis
B
Low
High
Contact frequency
Hi-M
Hi-C
Mb
15.3
15.6
C
5
0
-5
Normalized frequency
D
100
50
0
-50
-100
Normalized distance, nm
E
Pre-MBT
F
G
H
I
MBT
J
K
L
inter-TAD
TAD-1
TAD-2

Figure 4

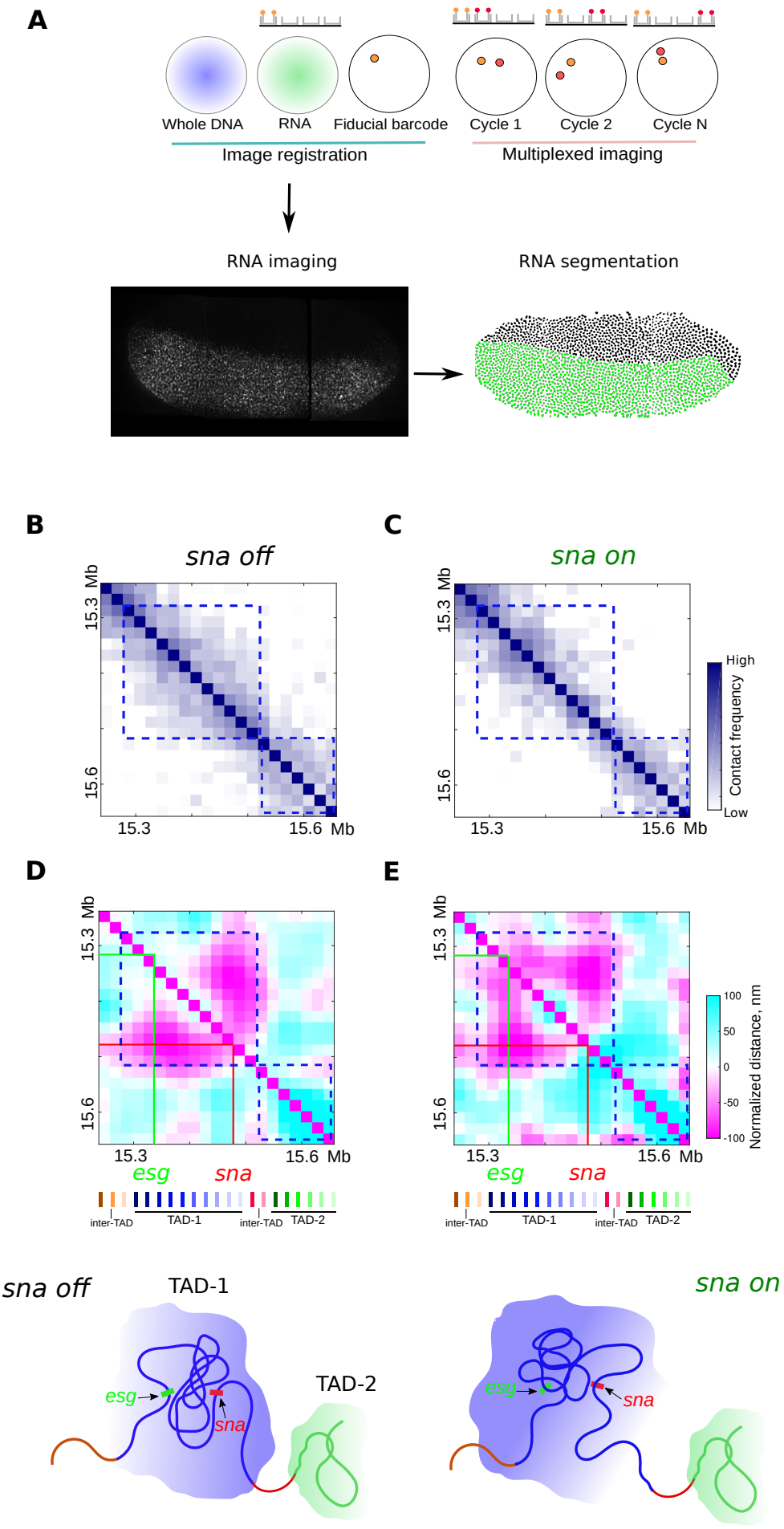
A
Whole DNA
RNA
Fiducial barcode
Cycle 1
Cycle 2
Cycle N
Image registration
Multiplexed imaging
RNA imaging
RNA segmentation
B
sna off
C
sna on
15.3 Mb
15.6
15.3
15.6 Mb
High
Contact frequency
Low
D
E
esg
sna
inter-TAD
TAD-1
TAD-2
100
50
0
-50
-100
Normalized distance, nm
sna off
TAD-1
TAD-2
esg
sna
sna on